



Driving fiber diameters to the limit: nanoparticle-induced diameter reductions in electrospun photoactive composite nanofibers for organic photovoltaics

R. M. Schofield¹ · B. M. Maciejewska¹ · S. Dong¹ · G. T. Tebbutt¹ · D. McGurty¹ · R. S. Bonilla¹ · H. E. Assender¹ · N. Grobert¹

Received: 23 September 2023 / Revised: 20 October 2023 / Accepted: 5 November 2023 / Published online: 13 December 2023
© The Author(s) 2023

Abstract

Electrospun photoactive nanofibers hold significant potential for enhanced photon absorption and charge transport in organic photovoltaics. However, electrospinning conjugated polymers with fiber diameters comparable to exciton diffusion lengths for efficient dissociation, is difficult. Previously, spinning sub-100 nm poly(3-hexylthiophene) (P3HT) fibers has required the auxiliary polymer, poly(ethylene oxide) (PEO), and large antisolvent additions. Therefore, its success differs considerably across donor polymers, due to variable antisolvent addition limits before precipitation. Herein, plasmonic nanoparticle infusion into P3HT nanofibers is used to modulate viscosity and deliver a novel and unrivaled strategy to achieve reduced fiber diameters. Following PEO removal, the fibers measure 55 nm in diameter, 30% lower than any previous report – providing the shortest exciton diffusion pathways to the heterojunction upon electron acceptor infiltration. The nanoparticle-containing nanofibers present a 58% enhancement over their pristine thin-film counterparts. ~17% is ascribed to plasmonic effects, demonstrated in thin-films, and the remainder to along-fiber polymer chain alignment, introduced by electrospinning. The anisotropy of light absorbed when polarized parallel versus perpendicular to the fibers increases from 0.88 to 0.62, suggesting the diameter reduction improves the alignment, resulting in greater electrospinning-induced enhancements. Controlled by the electrospinning behavior of PEO, our platform may be adapted to contemporary donor-acceptor systems.

Keywords Photovoltaics · Electrospinning · Nanofibers · Absorption enhancements · Polymer alignment

1 Introduction

Meeting the ever-expanding energy demand of society is among the greatest issues of our time. However, the most pressing concern is not our ability to harvest the energy to accommodate this, but to do so while limiting the environmental impact. Photovoltaic (PV) technologies provide a renewable energy source to contribute towards this goal, and emerging thin-film photovoltaics, including organic photovoltaics (OPVs), offer a promising alternative to silicon devices - being low cost, lightweight, and compatible with flexible substrates.

The conventional bulk heterojunction (BHJ) OPV features a blend of an electron-donating polymer and an electron acceptor which undergo nanoscale phase separation to produce a highly interconnected architecture with bicontinuous pathways [1]. For effective dissociation into free charge carriers, domains should be small enough so that excitons are formed within one exciton diffusion length of the heterojunction (~10 nm). Control over the thermodynamically unstable phase separation is limited beyond thermal [2–4] or solvent annealing, [5–7] and the BHJ morphology can suffer from isolated domains, [8] inefficient transport pathways, and a build-up of space charge due to charge mobility imbalance [9].

The BHJ is the dominant active layer architecture for polymer-based OPVs and typically exhibits optimal efficiency when 100 – 200 nm thick, due to the trade-off between light harvesting and charge extraction [1, 9]. Whilst this figure is significantly larger than the optimal thickness presented by a simple bilayer junction, the BHJ

✉ N. Grobert
nicole.grobert@materials.ox.ac.uk

¹ Department of Materials, University of Oxford, Parks Road, Oxford OX13PH, UK

still contains insufficient material to harvest the full intensity of incident light [9, 10]. Therefore, a major area of OPV research has focused on increasing optical absorption for the same volume of photoactive material.

One successful approach to increasing light harvesting is the electrospinning of photoactive polymer nanofibers. Electrospinning is a facile and tuneable method of producing continuous nanofibers over a large area [11] (in our case, 100 – 200 cm² with a single nozzle), with low material wastage, and potential compatibility with roll-to-roll processing [12, 13]. Electrospun photoactive nanofibers may be either incorporated into BHJ-OPV devices, [14, 15] or used to produce an alternative active layer architecture by infiltrating the interstitial space of the nanoweb with an electron acceptor [16–18]. The spinning process induces polymer chain alignment along the fiber axis, which can template the formation of highly crystalline polymer [19]. In the nanoweb, the fibers lie flat on the collector which translates into an increased proportion of polymer chains orientated parallel to the substrate, promoting increased light harvesting [14, 15, 20]. Extended conjugation lengths, resulting in a red-shift of the light absorption, are often reported to increase light absorption further, [14, 15, 19] and can provide improved overlap with solar emission [21]. Thirdly, the crystallinity and alignment could allow for greater hole mobility and therefore improved charge collection. Resultantly, there have been several instances of improved device efficiency upon nanofiber introduction [14–16].

Polymer entanglement is a prerequisite to effective electrospinning, needed to provide sufficient viscosity to impede beading and produce uniform fiber morphologies. Conjugated polymers typically do not fulfill this requirement, due to their rigid-rod behavior in solution. Even so, the electrospinning of this class of polymers has been achieved using high concentrations or a solvent sheath [22, 23]. Alternatively, fibers can be more easily electrospun through the addition of a ‘spinnable’ auxiliary polymer, such as high molecular weight poly(vinylpyrrolidone) (PVP), [24] PEO, [16–19, 21, 25–28] or poly(ϵ -caprolactone) (PCL) [14, 22]. These random-coil polymers may be either blended into the spinning solution alongside the conjugated polymer or used as the sheathing solution in a coaxial spinning set-up. However, the generated fibers are thick, measuring 200 nm to several microns in diameter, [14, 23, 24] and thus are ill-suited for OPV applications. Within a nanofibrous active layer architecture, the diameter of the photoactive nanofibers is directly linked to the probability of exciton dissociation. Therefore, the second challenge is to spin ideally thin photoactive nanofibers, with diameters comparable to twice the exciton diffusion length (~20 nm), or to produce a domain of this size following interdiffusion with the electron acceptor upon infiltration.

One successful strategy for reducing achievable diameters involves the addition of a polar co-solvent, of dimethylformamide (DMF):acetic acid [19]. The spinning solutions of conjugated polymers are typically non-conductive, and the solvent, often chloroform, possesses a low dielectric constant of 4.81. Therefore, co-solvent addition delivered a diameter reduction attributed to an increase in solution conductivity up to 0.35 $\mu\text{S cm}^{-1}$, [19] which likely allowed the first onset of bending instability during spinning to occur closer to the needle [29, 30]. This approach was used to electrospin sub-100 nm P3HT nanofibers (80 nm), and the first instance of a photoactive nanofiber, in this case, poly[N-9'-hepta-decanyl-2,7-carbazole-*alt*-5,5-(4',7'-di-2-thienyl-2',1',3'-benzothiadiazole)] (PCDTBT), with a diameter approximately twice that of the exciton diffusion length of the material, at 20 nm [16]. However, co-solvent additions were limited to 13.3 wt%, else the fibers became heavily beaded, which would lead to excessive recombination. During replication studies, we found that similarly sourced P3HT precipitated significantly at additions above 5 wt% DMF, limiting the obtainable fiber diameter to >200 nm. Therefore, even with the same polymer, the success of this approach can vary considerably, and other donor polymers may be more intolerant of antisolvent addition, limiting its application.

An alternative technique to increasing light harvesting involves the addition of noble metal nanoparticles (NPs). These nanostructures may enhance light harvesting through scattering, increasing the pathlength of light through the active layer, [31, 32] or, the local surface plasmon resonance (LSPR) effect, where the plasmonic near-field increases the effective absorption cross-section and exciton dissociation probability of the photoactive material [33, 34]. The nanoparticles can also create conduction pathways which can improve device efficiencies due to increased charge mobility [34, 35]. Interestingly, the addition of AgNO₃ into aqueous PEO spinning solutions, and the subsequent reduction of Ag⁺ ions by PEO to produce AgNPs in situ, [36, 37] hereafter referred to as PEO-reduced AgNPs, is reported to lower the diameters of PEO nanofibers by 30%, ascribed to increased electrical conductivity of the spinning solution [36]. In another report, effective AuNP dispersion was demonstrated within 120 nm P3HT nanofibers, by coaxial electrospinning with a PMMA sheath for transistor applications [38].

Herein, we produce ultra-thin P3HT nanofibers by monoaxial electrospinning in combination with PEO, and plasmonic silver or gold nanoparticles. Revealed by Scanning Electron Microscopy (SEM) and Atomic Force Microscopy (AFM) studies, we describe an innovative nanoparticle-induced fiber diameter reduction capable of producing 55 nm fibers, 30% lower in diameter than any prior report [19]. By investigating the influence of nanoparticles

within PEO electrospinning solutions and resulting nanofibers, we successfully elucidate the mechanism for achieving unparalleled fiber diameters. Driven by time-dependent modulation of the spinning solution, the nanoparticles induce diameter reductions by delivering a unique decrease in viscosity alongside increased electrical conductivity.

Through absorption spectroscopy, it is revealed that the light harvesting properties of the P3HT nanofiber-based films show strong dependence upon the fiber diameter. Evaluated by the absorption of parallel and perpendicularly polarized light, we ascribe this to the variable extent of polymer alignment along the fiber axis. Through these relations, we provide deeper insight into the link between polymer processing, preferential orientation and photon absorption.

By comparing the absorbance of pristine and nanoparticle-containing P3HT nanofibers and thin-films, we deconvolute the relative contributions of electrospinning-induced polymer chain alignment, and plasmonic effects from the nanoparticles. Combined, these synergistic effects provide up to 1.58x superior light harvesting over conventional spin-coated thin-films.

2 Results and discussion

2.1 Diameter-dependent light harvesting

Figure 1a schematically presents the preparation of nanoparticle-containing P3HT nanofibers by electrospinning P3HT/PEO solutions. The digital photograph shows a dark purple mat of P3HT/PEO nanofibers, also in Fig. 1b, presenting their strong light harvesting ability and free-standing nature at this stage. The as-spun fibers are subsequently heated in isopropanol (IPA) to remove the insulating PEO. The resultant P3HT fibers in Fig. 1c-f, are highly textured, continuous for several microns, and apparently fused at the junctions between fibers. After PEO removal, the lowest achieved dimensions of these fibers were found to be 55 nm in height and 95 nm wide on the ITO-coated glass substrate. Thinner fibers should be capable of delivering more effective exciton dissociation after [6,6]-phenyl-C₆₁-butyric-acid-methyl-ester (PCBM) infiltration, as excitons will be produced closer to the surface. Here, our fibers provide exciton diffusion pathways of ≤ 28 nm, even before interdiffusion is considered.

Due to strong light scattering by the nanoweb, optical absorbance was determined by measuring the total reflectance and transmittance using an integrating sphere. Combination of these measurements determines a near-zero absorbance beyond 700 nm, indicating successful consideration of diffuse scattering in these measurements (see Fig. S1).

In Fig. 1g, SEM studies in conjunction with statistical analyses revealed a time-dependent reduction in the diameters of P3HT/PEO fibers upon PEO-reduced AgNP introduction. The as-spun diameters drop from 240 nm to 100 nm, as the spinning solution was aged for up to 96 h prior to electrospinning. We later investigate the mechanism behind this reduction in depth using PEO nanofibers. Presented in Fig. 1h and S2a, after the nanoparticle introduction, the absorbance of the nanofiber-based films increases with the solution aging time before spinning. The absorbance peaks after 72 – 96 h, which correlates well with the minimum diameter of the spun fibers. Fibers electrospun immediately after nanoparticle addition to the spinning solution (0 h aging), offer a maximum light harvesting at 560 nm of 45%. The same mass of thinner fibers spun after 72 – 96 h, delivers 83% absorbance at this wavelength. Beyond 96 h, we observe the onset of fiber beading, which coincides with the observed drop in absorbance to 71% at 168 h.

The first reason for this time-dependent light harvesting improvement can be attributed to the PEO-reduced AgNPs forming in solution over time, contributing to LSPR enhancements (see Fig. S2b). However, we also identify that the degree of electrospinning-induced polymer alignment is linked to the fiber diameter, which decreases with aging time of the nanoparticle-containing solution. The extent of polymer chain alignment was determined for fiber samples of varying diameters - pristine P3HT nanofibers, and PEO-reduced AgNP-containing P3HT nanofibers electrospun after the spinning solution was aged for 24 and 96 h. Prior to PEO removal, these fibers possess diameters of 230 ± 56 , 162 ± 41 , and 99 ± 27 nm, respectively. The fibers in each sample were orientated along a common axis using a rotating drum collector (see Fig. S1e).

In Fig. 1i-j, the absorption by the samples was greater when the incident light was polarized along (parallel) versus polarized across (perpendicular to) the fiber axes. This anisotropy indicates the chains are generally orientated along the axis of the nanofiber. This is because excitation of the polymer is dependent upon the orientation of the transition dipole moment with respect to the polarization of light, with a higher probability of absorption when the polymer backbone and the electric field of light are similarly orientated [18]. In Fig. 1i, aligned pristine P3HT nanofibers possess a 0-1 transition (560 nm) absorbance (A) ratio with parallel (\parallel) and perpendicularly (\perp) polarized light of $A_{\perp}/A_{\parallel} = 0.88$. The nanoparticle-containing fibers spun after 24 h of aging, with an intermediate diameter, gave a $A_{\perp}/A_{\parallel} = 0.79$ (see Fig. S1c). Meanwhile, in Fig. 1j, the thinner PEO-reduced AgNP-containing P3HT nanofibers spun after 96 h, showed greater polarization dependence, with a ratio of 0.62. In Fig. S1a, a randomly orientated fiber mat spun onto a static collector, showed no dependence with polarized light ($A_{\perp}/A_{\parallel} = 0.99$).

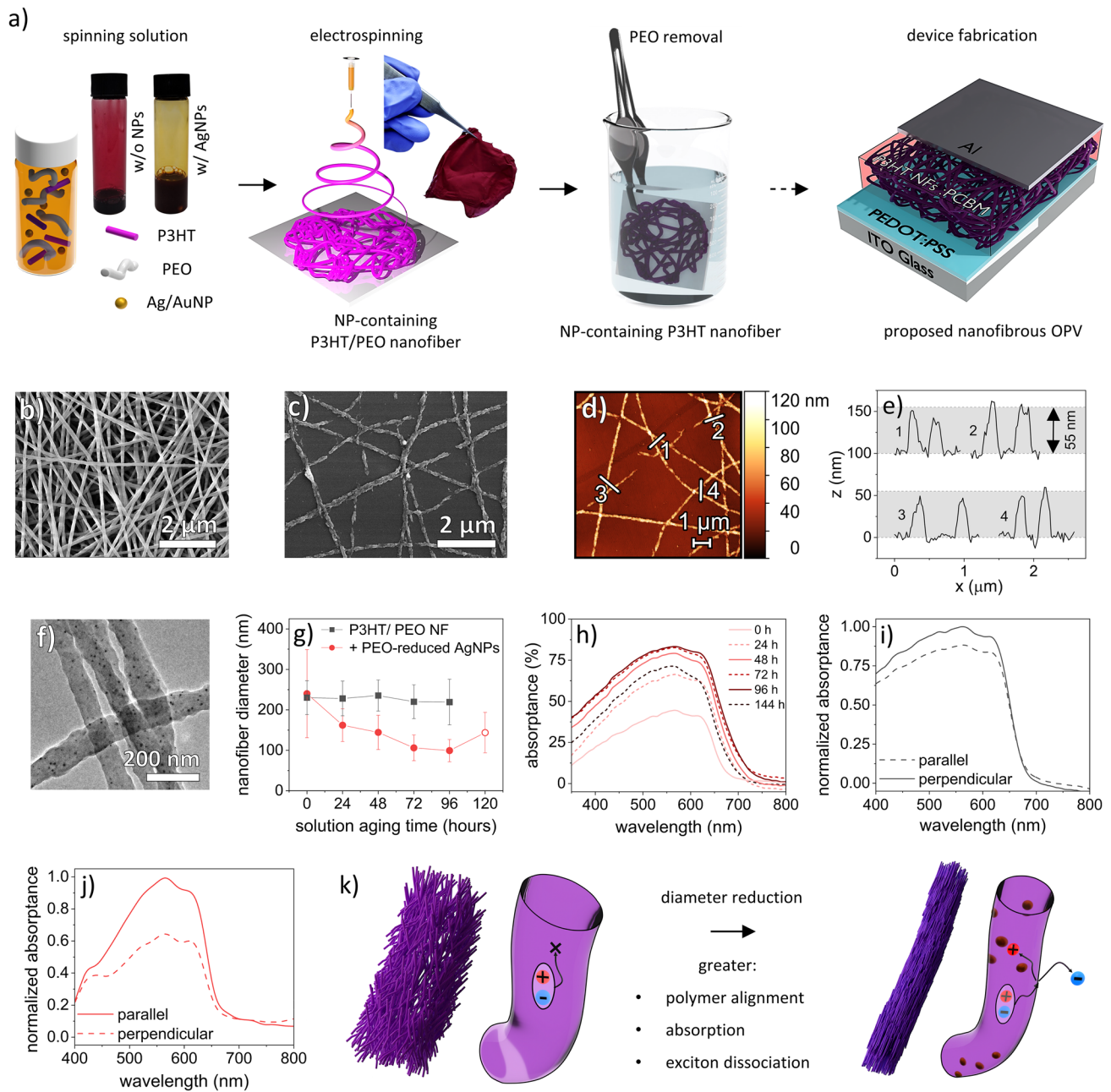


Fig. 1 a) Schematic of the preparation of NP-containing P3HT nanofibers, and structure of the proposed nanofiber-based OPV device. Inset: Optical photograph of a free-standing P3HT/PEO nanoweb. SEM micrographs of **b)** 100 nm NP-containing P3HT/PEO nanofibers electrospun from a solution containing 0.35 wt% PEO, 0.25 wt% P3HT and 10 wt% AgNO₃ (wrt PEO) in chloroform: DMF (95:5 w/w) and **c)** the NP-containing P3HT nanofibers following PEO removal with hot IPA, revealing a final width of 95 nm (spinning solution contained 0.15 wt% P3HT). **d)** AFM image and **e)** extracted profiles of the washed fibers in (c) revealing a vertical dimension of 55 nm. **f)** TEM micrograph of the NP-containing P3HT nanofibers, showing effective dispersion of the NPs. **g)** Reduction in P3HT/PEO fiber diameters achieved by NP addition and aging of the spinning solution (symbol without fill indicates a beaded fiber). **h)**

Absorbance spectra of the PEO-reduced AgNP-containing P3HT nanofibers spun over time, showing an absorbance increase until 72–96 h. Beaded fibers are spun beyond this stage, coinciding with decreased absorption. Polarized absorbance spectra of **i)** P3HT nanofibers and **j)** PEO-reduced AgNP-containing P3HT nanofibers aligned using a drum collector, spun after 96 h aging, with light polarized along (parallel) and across (perpendicular) the fiber axes. Higher absorption of parallel-polarized light indicates that the polymer chains are aligned along the fiber, and that alignment improves with NP addition and the fiber diameter reduction. **k)** Schematic illustration of diameter-dependent polymer chain alignment along the fiber axis introduced by electrospinning, and the importance of thin fibers in providing short exciton diffusion pathways to the heterojunction upon electron acceptor infiltration

These observations cannot be explained by differences in the extent of fiber orientation in a common direction by the rotating collector, as we would expect the thicker fibers to be shorter for a given volume, and so better aligned under the same drum rotation speed. Instead, we reveal that polymer chain alignment along the fiber axis improves with a reduction in the fiber diameter. This is logical as lower diameter fibers will have undergone a greater degree of uniaxial elongation during fiber flight to have reached this size, and similarly the polymer chains are stretched out in this direction, as communicated by Fig. 1k.

Along-fiber alignment leads to a greater degree of polymer orientated parallel to the substrate upon fiber collection. This in-plane configuration delivers greater absorption, as more polymer is orientated so that the π - π^* transition dipole moment (along the backbone) has an effective overlap with the electric-field vector of the incident light, approximately normal to the substrate [14, 15, 20]. This, along with an increasing plasmonic intensity, and longer light pathlengths due to scattering by the larger fiber surface area, results in greater light harvesting by fibers spun from aged solutions. Further optical analysis is conducted to deconvolute plasmonic and alignment-associated absorption enhancements as described later.

2.2 Reducing achievable nanofiber diameters

Although polymer chain entanglement is essential for effective electrospinning, viscosity provides resistance to the elongation forces acting on the forming fiber, reducing the stretching and thinning of the jet. Therefore, one must use the lowest possible polymer concentration when attempting to produce the thinnest achievable nanofibers. However, when the concentration is too low, surface tension forces will dominate, leading to beading to minimize the surface energy, or the jet breaks into droplets, i.e., electrospaying. From a chloroform solution, the concentration of 900 kDa PEO must be greater than 0.50 wt% to avoid beading, yielding approximately 500 nm fibers. In the presence of a polar co-solvent, the beading onset concentration is reduced to 0.35 wt% [19]. Kim et al. suggested 100 nm fibers are spinnable with 9.4 wt% DMF and 3.9 wt% acetic acid. However, in Fig. 2a, the minimum PEO fiber diameter spun within this work in the absence of nanoparticles was 140 nm, using 8 wt% DMF. Further additions of DMF, or acetic acid, were found to lead to beading (see Fig. S3).

Stable additions of up to 10 wt% AgNO_3 wrt the PEO concentration could be made to 0.35 wt% PEO solutions in chloroform: DMF (92: 8 w/w) before aggregation. The DMF addition was used to solubilize the AgNO_3 . After reduction, and the formation of PEO-reduced AgNPs, we obtain a nanoparticle-containing spinning solution via a 'one-pot' synthesis. Upon electrospinning, silver addition

was demonstrated to reduce the diameter of PEO nanofibers by over 40%, with our champion nanoweb possessing a diameter of 75 ± 17 nm, as shown in Fig. 2b and c. To the best of our knowledge, this presents the lowest diameter of PEO nanofibers spun from a chloroform-based solution. Diameter reductions were found to occur even with very low nanoparticle additions, although the reduction slowed above 0.1 wt% AgNO_3 wrt PEO.

In Fig. S4, the incorporation of nanoparticles was not found to induce any change in the surface tension of the spinning solution. However, the electrical conductivity of the solution in Fig. 2c was found to rise linearly with AgNO_3 addition, up to $10 \mu\text{S cm}^{-1}$. The contribution by the nanoparticles towards greater conductivity has not been elucidated, however, we expect it can be largely ascribed to residual Ag^+ and NO_3^- ions as they possess higher mobility and charge density. Oleylamine-capped nanoparticles (OA-capped NPs) produced a significantly smaller enhancement in electrical conductivity due to the lower concentration of residual ions, the larger nanoparticle size and hence lower mobility, and the insulating capping layer (see Fig. S5). However, in Fig. 3b, similar diameter reductions could be observed as a result of the presence of these nanoparticles, suggesting that the higher conductivity of the precursor solution is not the sole or primary reason for the decreasing diameter.

Figure 2d also reveals the addition of nanoparticles has a considerable influence on the viscosity of a 1.5 wt% PEO solution, which correlates well with the decreasing diameter. We initially considered that this may be due to PEO adsorbing to the nanoparticles, reducing the proportion of 'free' polymer contributing to the viscosity. However, OA-capped NPs also delivered a viscosity reduction despite their dense capping layer, (see Fig. S6) and upon isolating the nanoparticles from the spinning solution after 48 h by centrifugation, we found no evidence of PEO capping or displacement of the oleylamine ligands, as investigated by Fourier Transform Infrared Spectroscopy (FTIR) in Fig. S7. Instead, there is evidence that sufficiently small gold nanoparticles can lead to bulk rheological changes in PEO melts [39, 40]. Within that study, nanoparticles smaller than the matrix entanglement mesh size induced an increase in the reptation tube diameter of the polymer, reducing the viscosity of the composite melt. Therefore, we suggest that a similar response occurs within semi-dilute PEO solutions with the addition of ≤ 10 nm nanoparticles.

Lower viscosity reduces the resistance to fiber stretching, whilst the higher charge density enhances the elongation forces from the applied electric field, [29, 36] allowing for the production of thinner nanofibers. Further, without nanoparticles, the tapered linear section of the electrospinning jet spans >5 cm of the 20 cm needle-collector separation. Due to the increased instability after nanoparticle addition, the whipping onset could be observed to occur closer to the

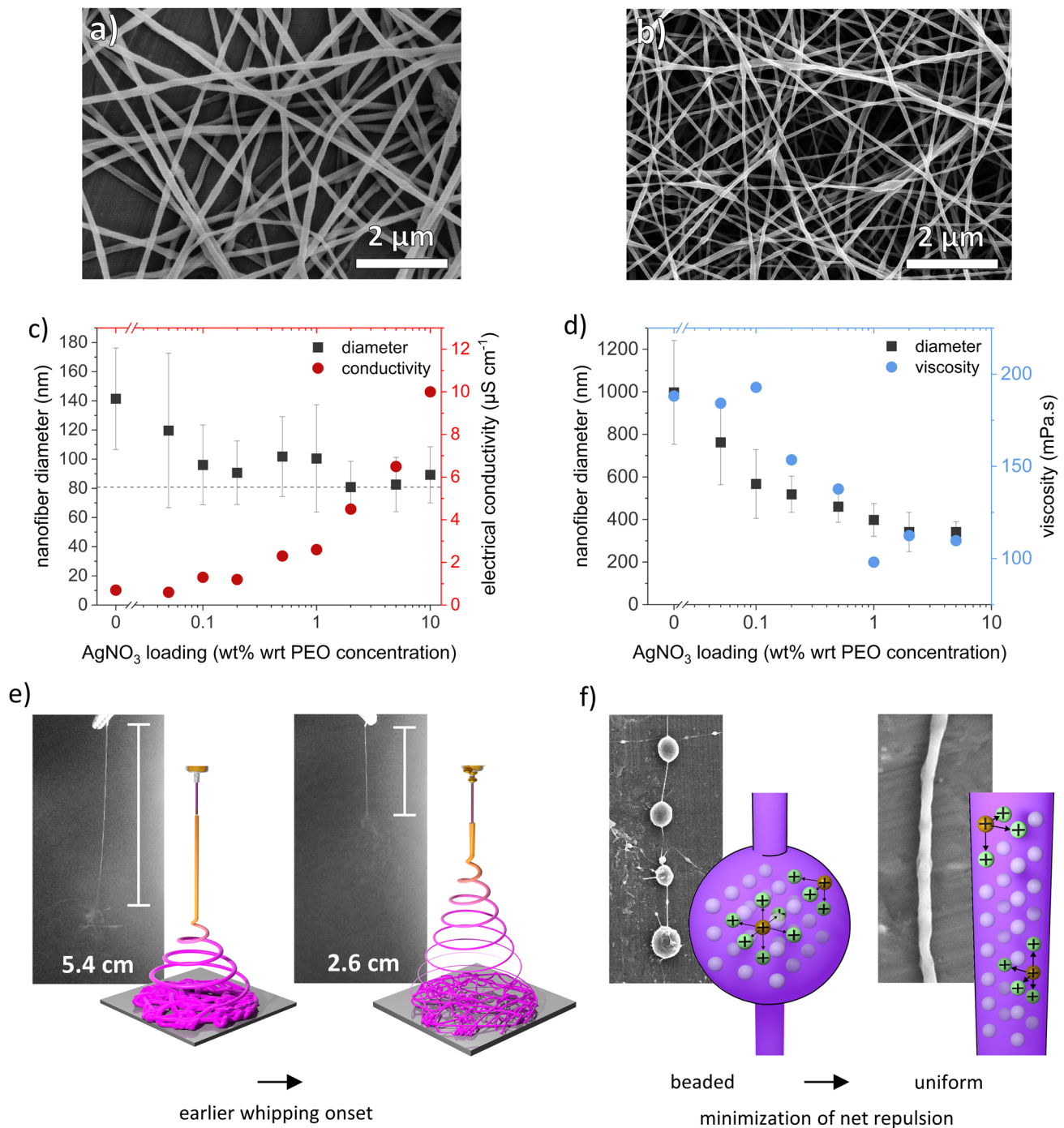


Fig. 2 SEM micrographs of **a)** PEO nanofibers and **b)** PEO-reduced AgNP-containing PEO nanofibers electrospun from solutions containing 0.35 wt% PEO, and in the latter case, 5 wt% (wrt PEO) AgNO_3 /PEO-reduced AgNPs. **c)** Enhanced electrical conductivity and reduction in PEO nanofiber diameters upon AgNO_3 /PEO-reduced AgNP addition to 0.35 wt% PEO solutions aged for 48 h. **d)** Viscosity and spun fiber reductions induced by AgNO_3 /PEO-reduced AgNP addition to 1.5 wt% PEO solutions aged for 72 h. **e)** Digital photograph and

diagram of the shorter linear jet section from NP addition, after which the majority of fiber elongation occurs, allowing for the electrospinning of thinner fibers. **f)** Example SEM micrographs of beaded and uniform PEO nanofibers, and corresponding schematics of the proposed mechanism for achieving uniform fiber morphologies from low viscosity NP-containing solutions – the fiber adopts a morphology with higher surface area to minimize the repulsion between the higher density of charged species

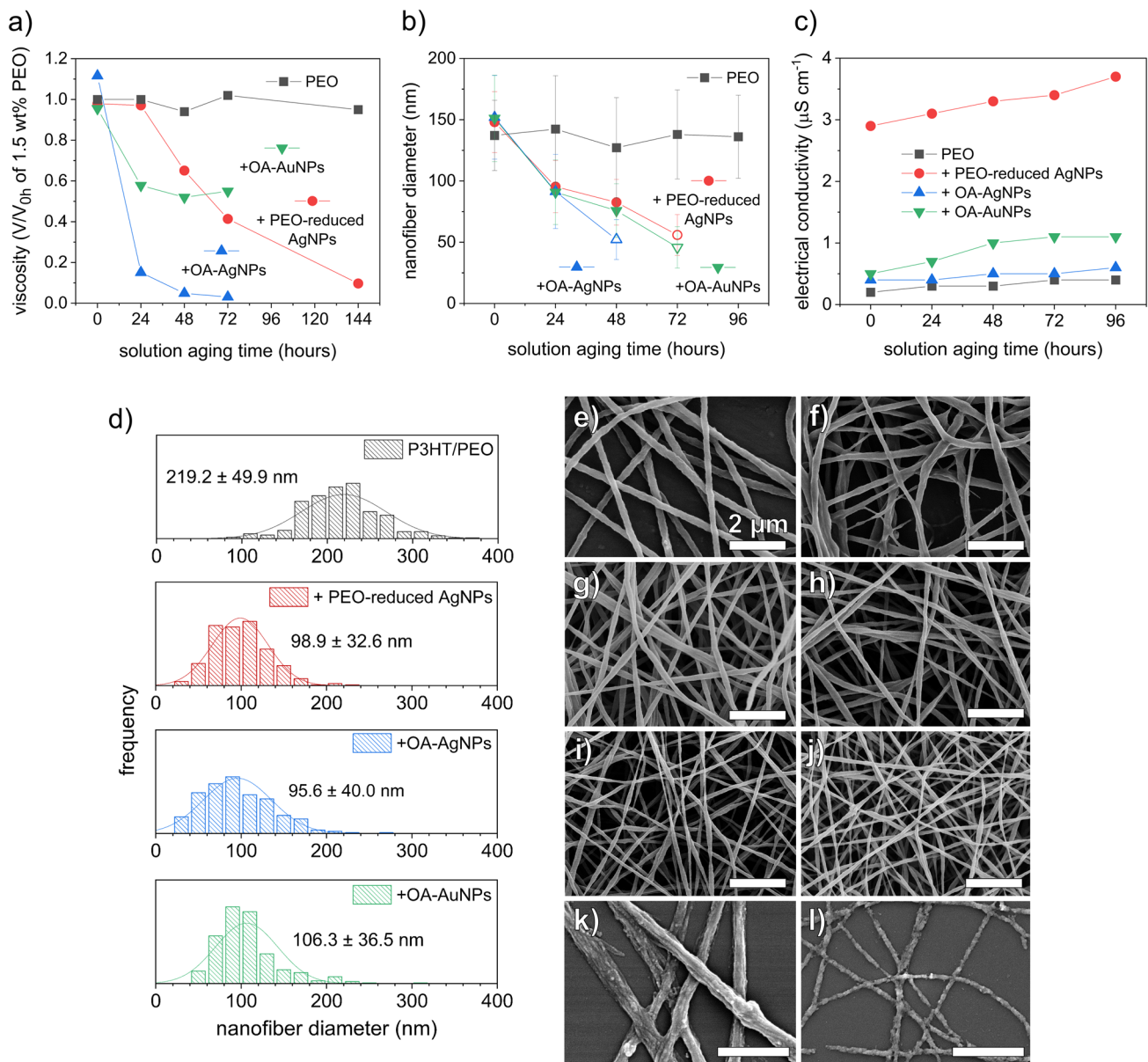


Fig. 3 a) Dynamic viscosity reduction of a 1.5 wt% PEO solution containing 2 wt% (wrt PEO) AgNO_3 /PEO-reduced AgNPs or OA-capped NPs. b) PEO and 5 wt% (wrt PEO) NP-containing PEO nanofiber diameters spun as the spinning solution ages, presenting time-dependent diameter reductions after NP addition (symbols without fill indicate beaded fibers). c) Electrical conductivity of a 0.35 wt% PEO solution over time containing 5 wt% (wrt PEO) AgNO_3 /PEO-reduced AgNPs or OA-capped NPs. d) Histograms

showing the diameter distribution of P3HT/PEO nanofibers containing 10 wt% (wrt PEO) nanoparticles, spun after 92 h aging. OA-capped NP-containing fibers were spun in the absence of DMF addition to the spinning solution. SEM micrographs of e) P3HT/PEO nanofibers and f) - j) PEO-reduced AgNP-containing P3HT/PEO nanofibers aged for f) 0 h, g) 24 h, h) 48 h, i) 72 h and j) 96 h. k) P3HT nanofibers and l) the NP-containing P3HT nanofibers after PEO removal (scale bars: 2 μm)

needle, within 3 cm, seen in Fig. 2e and S8. Initially, the electrospinning jet travels almost directly from the needle to the collector. Following the first coiling event, the trajectory of the jet has a significant outward component and travels approximately perpendicular to the previous linear jet section [29]. The overall pathlength of the jet in flight increases exponentially with each successive bending instability,

and therefore a majority of fiber stretching occurs after the first instability. By producing an earlier whipping onset, we suspect that the fiber pathlength increases further, and therefore nanoparticle addition can provide a longer time for elongation before either the solvent evaporates (which prevents further thinning), or the fibers are collected at the ground plate.

The fiber uniformity was also improved with fewer beads observed. Whilst in the absence of nanoparticles, a PEO solution at this reduced viscosity would produce highly beaded fibers, the nanoparticles appear to impede beading [36]. We theorize that this may be attributed to a higher density of repulsive charges from residual ions and charges generated on the nanoparticles when the voltage bias is applied. As conveyed in Fig. 2f, this would favor the production of uniform fiber morphologies, which possess a higher surface area to volume ratio to minimize repulsion between charged species during fiber flight.

This reduction in viscosity is in fact a dynamic process, with significant reductions measured beyond 24 h. In Fig. 3a, we present a continuous reduction in viscosity as the spinning solution ages. The spinning solution viscosity can reduce by >90%, producing thinner fibers as the solution ages, and beyond a critical aging time, the solution does not possess the necessary entanglement for uniform fiber formation, and beading begins to occur, as demonstrated in Fig. 3b. Later still, the solution is electrospayed. The aging time required for this onset (typically 24 - 48 h) is dependent upon the type and loading of the nanoparticle, and initial viscosity of the solution. Until 24 h, the viscosity of the PEO-reduced AgNP-containing solution was stable due to the time taken for the reduction of the silver salt. With separately synthesized OA-capped NPs, the viscosity has already decreased significantly by 24 h. Interestingly, we found OA-capped AuNP addition provided a lesser reduction, which plateaued beyond 24 h.

Electrical conductivity was also found to increase over time, aiding the production of thinner fibers. Figure 3c shows a $0.8 \mu\text{S cm}^{-1}$ increase in the PEO-reduced AgNP-containing solution corresponding to a 27% change, while the relative increases in OA-capped NP solutions were 50% and 120% for AgNP and AuNP analogues, or 0.2 and $0.6 \mu\text{S cm}^{-1}$. Conductivity likely increases due to the reducing viscosity, which allows for higher mobility of charged ions and nanoparticles in solution. However, it should be noted the pristine PEO solution also increased from 0.2 to $0.4 \mu\text{S cm}^{-1}$ over 96 h, perhaps due to improved solvation, but fiber diameters were stable over this period. Furthermore, if conductivity were the major factor determining the fiber diameter, we would expect thinner fibers to be produced immediately after nanoparticle addition (hour 0), as the electrical conductivity has already significantly increased.

We conclude that the mechanism for diameter reduction in PEO-based nanofibers upon nanoparticle addition, is primarily due to a reduction in viscosity, and enhanced electrical conductivity may act as a secondary factor, although perhaps necessary to maintain uniform fiber morphology.

2.3 Towards ideal P3HT nanofibers

As PEO dominates the electrospinning behavior of P3HT/PEO fibers, we find analogous diameter reductions upon P3HT addition. As previously described, in Figs. 1g and 3d-l, the reduction in diameter is easily observed. At additions of 10 wt% AgNO_3 wrt PEO, sub-100 nm nanofibers could be spun from a 0.35 wt% PEO/ 0.25 wt% P3HT spinning solution in chloroform: DMF (95: 5 w/w), when aged for 96 h. It was necessary to limit DMF addition to 5 wt% to prevent beading and precipitation of P3HT, yielding a lowest spinnable diameter of P3HT/PEO without nanoparticle addition of 220 nm.

The mechanism for diameter reduction is independent of DMF addition, yet it is still required to solubilize AgNO_3 . In contrast, when using separately synthesized OA-capped Ag and AuNPs, which have previously shown enhanced exciton generation in plasmonic OPV devices, [41] we deliver a similar and significant diameter reduction in the absence of any antisolvent addition, as in Fig. 3d.

Due to P3HT addition and therefore higher initial viscosity, the optimal aging time to produce the thinnest uniform fibers was extended until 96 h. Lowering the P3HT content reduced diameters further, and the optimal aging time decreased accordingly. At 0.15 wt%, 85 nm fibers were spun at 72 h, and at <0.10 wt% P3HT, 80 nm fibers were produced after 48 h (see Fig. S9).

Brunauer-Emmett-Teller (BET) analysis revealed that the specific surface area of the as-spun P3HT/PEO nanofibers doubled upon 10 wt% AgNO_3 addition and 96 h aging, from $5.55 \pm 0.08 \text{ m}^2/\text{g}$ to $11.79 \pm 0.13 \text{ m}^2/\text{g}$, therefore indicating the potential for increased heterojunction surface area, and thus, exciton dissociation, upon backfilling the nanoweb with an electron acceptor (see Fig. S10).

Due to the insulating nature of PEO, if it is not effectively removed by selective dissolution in hot IPA, it would significantly hamper exciton and charge carrier transport within the sample. Akin to previous works, [16, 19] a Thermogravimetric Analysis (TGA) isotherm at 370°C under nitrogen was employed to determine that ~1.5% of PEO remains from the washing procedure (see Fig. S11). At this temperature, PEO is almost completely degraded, however, P3HT has negligible weight loss. In the X-ray Diffraction (XRD) trace in Fig. 5a, the presence of PEO in the as-spun fibers is indicated by the peaks at 19.2° and 23.4° 2θ , indexed as the (120) and (112) reflections respectively, [42] which disappear entirely upon washing.

The material cost of the nanoparticles is substantial, therefore if a large proportion is lost upon washing, this would be undesirable. Comparison of TGA residuals at 900°C of washed P3HT and PEO-reduced AgNP-containing

P3HT fibers (solution contained 0.35% PEO and 0.25% P3HT) provides an estimate for the Ag content, from which we determine that ~80% of the nanoparticle mass was retained (see Fig. S12 and Table S1). This analysis was conducted in air to promote further degradation of the polymers than is possible under nitrogen, producing smaller, consistent residuals. As 55% of the fiber by mass (PEO) is removed during washing, 80% retention is considered acceptable.

For facile removal of PEO, the phenomenon first reported by *Kim et al.*, in which the polymers phase separate to form a

P3HT core and PEO sheath, attributed to a difference in viscosity, [19] is integral. The as-spun fibers herein also show a core-shell structure as in Fig. 4a. This favorable morphology avoids the production of isolated PEO domains which would be difficult to remove by solvent. Energy-dispersive X-ray spectroscopy (EDX) line scans across the P3HT/PEO fibers in Fig. 4b-c, show that nanoparticles do not prevent the migration of PEO towards the fiber surface, as indicated by the higher intensity of oxygen atoms for ~20 nm at the exterior of the fiber. Meanwhile, the sulfur count, proportional to

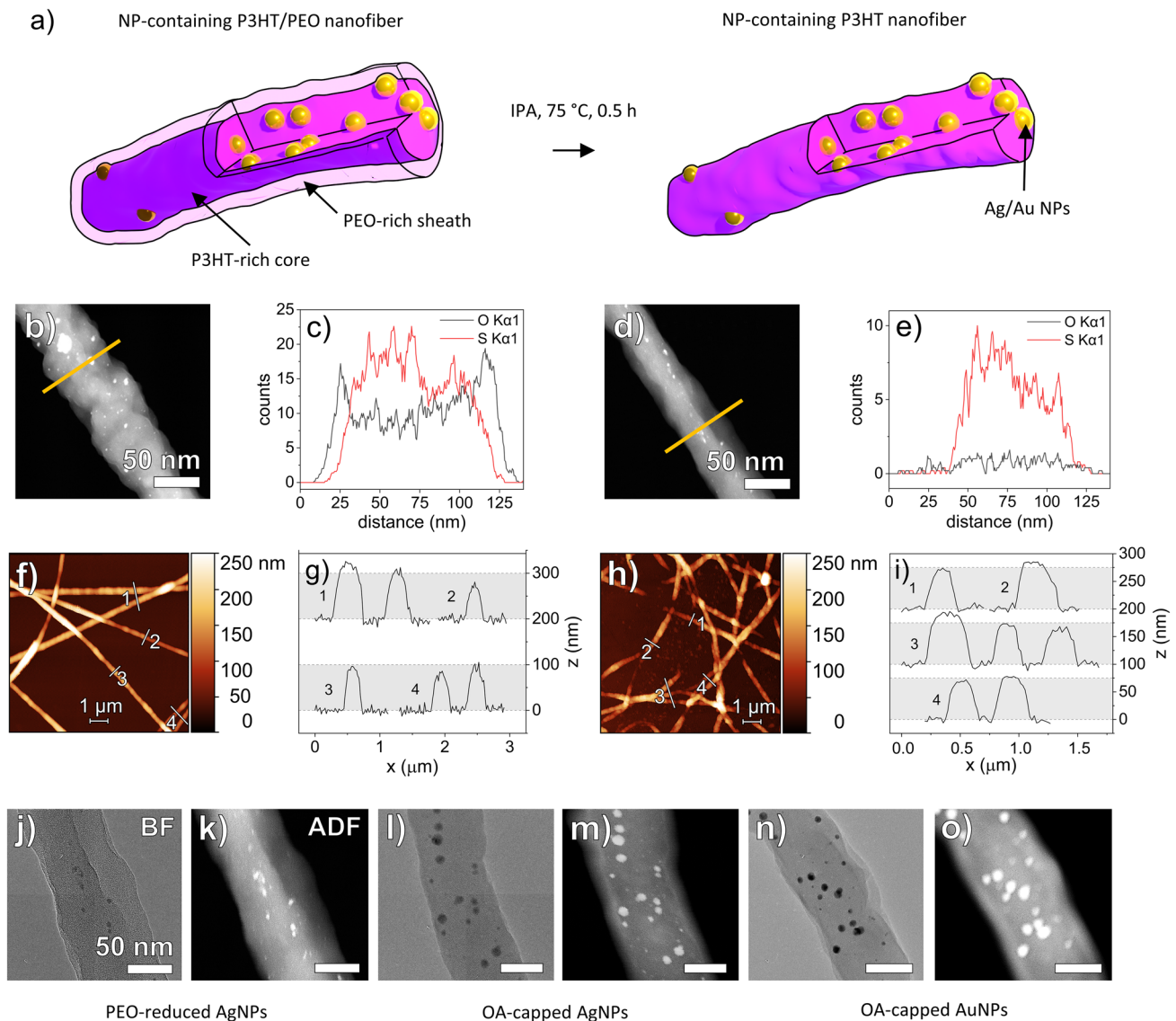


Fig. 4 a) Schematic of the as-spun and NP-containing P3HT nanofiber after PEO removal. b) – c) EDX line scan of an as-spun NP-containing P3HT/PEO nanofiber, showing phase separation between the O-rich polymer, PEO, and S-rich P3HT, producing a core-sheath structure. d) – e) EDX line scan of nanofiber after PEO removal. f) AFM scan and g) extracted height profiles of the as-spun fibers, revealing a vertical dimension of ~100 nm, consistent with SEM analysis. h) AFM scan

and i) extracted profiles of the washed fibers, revealing a reduction of the fiber height to 75 nm (spinning solution contained 0.25% P3HT). j, l, n) Bright field (BF) TEM and k, m, o) Annular Dark Field (ADF) Scanning TEM (STEM) micrographs of P3HT nanofibers containing effective dispersions of j, k) PEO-reduced AgNPs, l, m) OA-capped AgNPs and n, o) OA-capped AuNPs (scale bars: 50 nm)

the P3HT content, is absent for 10 nm, beyond which the sulfur count increases to a maximum towards the fiber core, as expected. EDX scans in Fig. 4d-e of the fiber post washing support the selective dissolution of the auxiliary polymer.

An uninterrupted P3HT core is equally important as it allows fibers to retain continuity as the PEO is dissolved. Prior to washing, the fibers were cylindrical, measuring 99 ± 33 nm in width and 98 ± 25 nm in height, as determined by SEM in Fig. 3j and AFM in Fig. 4f-g, respectively. During the washing procedure, the fibers ‘slump’, becoming 116 ± 33 nm wide and 73 ± 25 nm high, presented in

Figs. 3l and 4h-i. Lowering the P3HT content from 0.25 wt% to 0.15 wt% produced our smallest, optimized nanofibers as presented in Fig. 1c-f, at 96 ± 27 nm wide and 55 ± 13 nm high. Below 0.15 wt%, fibers became increasingly discontinuous upon PEO removal.

In Fig. 4j-o, Transmission Electron Microscopy (TEM) analysis shows an effective dispersion of nanoparticles along the length of the fiber. This is achieved due to the stability of nanoparticles in the spinning solution, and the surface charge of these particles providing repulsion during fiber formation.

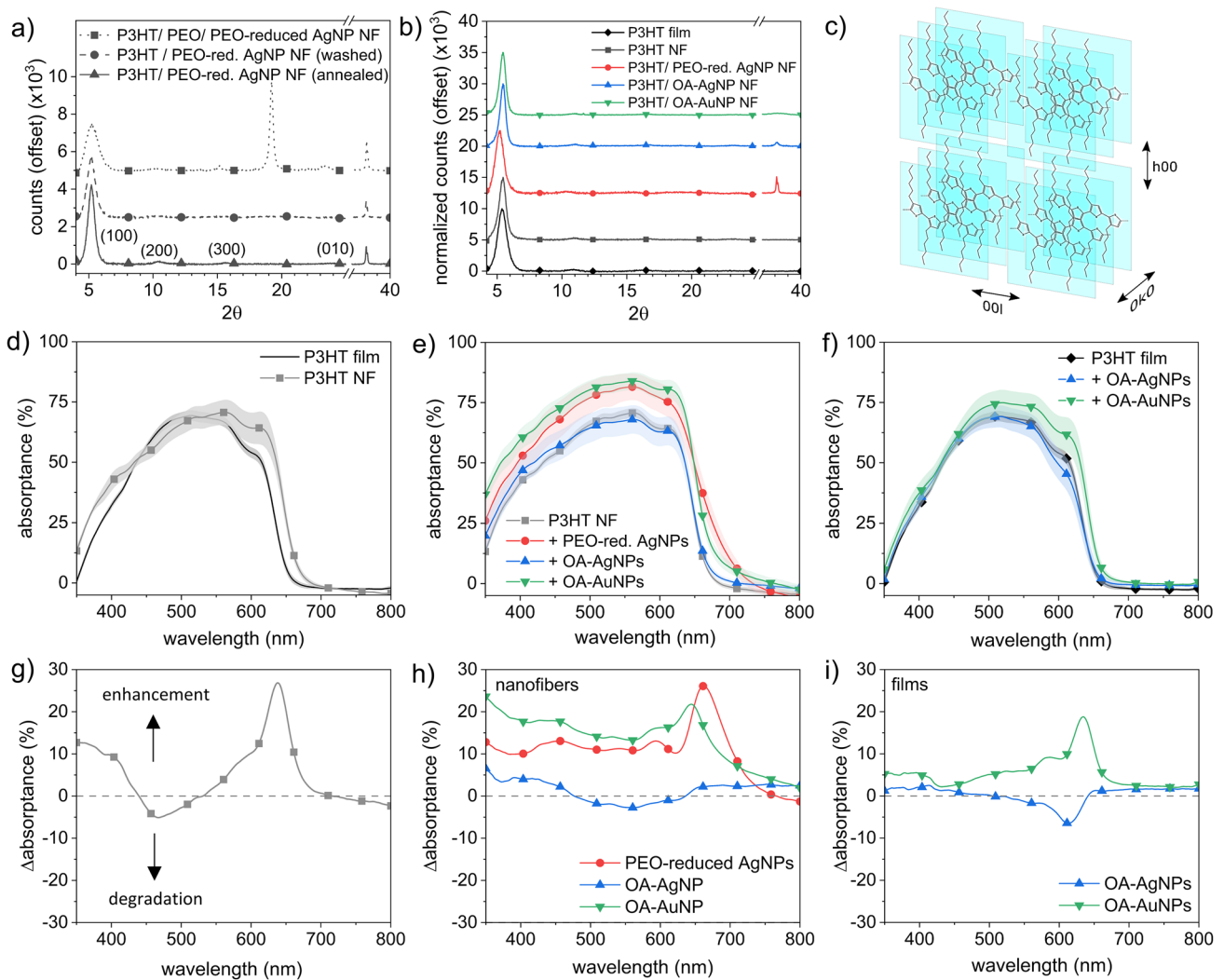


Fig. 5 XRD traces of **a)** the as-spun, washed and annealed PEO-reduced AgNP-containing P3HT nanofibers and **b)** P3HT films, and washed P3HT nanofibers and NP-containing P3HT nanofibers. **c)** Depiction of an ideal P3HT crystal showing diffraction axes. Absorbance spectra of **d)** electrospun P3HT nanofibers and spin-coated films, and NP-containing **e)** nanofibers and **f)** films, present-

ing dual absorption enhancement modes from electrospinning and plasmonic effects. Change in the absorbance spectra upon **g)** electrospinning P3HT in comparison to a spin-coated film, and upon NP addition to **h)** nanofibers and **i)** films compared to their pristine counterparts

2.4 Photoactive nanofiber performance

The lamellar spacing and size of crystallites was extracted from XRD traces to investigate the influence of electrospinning and nanoparticle presence (full details in Table S3). In Fig. 5a, the (100) reflection of P3HT manifests as a strong, broad peak at $5.51^\circ 2\theta$ in the diffractogram of as-spun PEO-reduced AgNP-containing P3HT/PEO nanofibers. From this, we can calculate a lamellar P3HT d-spacing of 1.70 nm and a crystallite size of 7 nm (estimated by applying the Scherrer equation). Upon washing, the crystallite size rises to 10 nm, due to the elevated temperature. Annealing at 120°C for 20 minutes leads to a further increase, to 12 nm. However, we see no evidence that the extent of crystallinity, proportional to the peak area, is increased by the post-processing steps. In contrast, the aromatic π - π stacking or (010) peak was only very weakly detected at $\sim 24^\circ 2\theta$.

Equivalent washed P3HT nanofibers without particles (Fig. S13a) possess a smaller d-spacing (1.63 nm) and larger crystallite size (12 nm). This suggests that PEO-reduced AgNPs may disrupt the stacking and interdigitation of the alkyl side chains, resulting in larger d-spacing and smaller crystallites. However, OA-capped NP-containing nanofibers in Fig. 5b presented more encouraging results, with greater crystallite sizes (15 nm and 13 nm for the Ag and Au analogues respectively) and the expected d-spacing (1.62 nm). Therefore, we do not find that the presence of nanoparticles systematically affects the nature of the crystallites.

Films spin-coated from a P3HT solution (in chloroform) and the PEO-reduced AgNP-containing spinning solution (Fig. S13b), produced similar d-spacings and crystallite sizes to the corresponding fibers. This is despite the greater size confinement and faster solvent evaporation rate during fiber formation over spin-coating. We envisage that polymer alignment prior to crystallization provides a templating effect for crystallite formation which can offset any disruption caused by the presence of the nanoparticles or the electrospinning process.

Comparison of the extent of crystallinity between each sample is not reliable, as the peak intensities will be affected by differences in crystallite orientations between samples. Thin-films will often adopt an ‘edge-on’ conformation, presenting the alkyl sidechains at the film-substrate and film-air interfaces, [43] whilst we anticipate that crystallites may be aligned along our fibers, giving rise to both ‘edge-on’ and ‘face-on’ configurations.

Revisiting the optical properties, we observe a change in the shape of the spectral absorbance upon electrospinning. Akin to previous reports with electrospun or self-assembled nanofibers of P3HT, [19, 44–46] the ratio between the first two vibronic peak intensities (0-0 /0-1 at ~ 615 nm and ~ 560 nm respectively) is enhanced relative to thin films, as in Fig. 5d. This is indicative of increased

J-aggregate behavior as described by Spano et al. [47, 48]. In thin films, P3HT usually possesses H-aggregate characteristics. The co-facial stacking favors interchain interactions, and excitons are delocalized between neighboring molecules. In this regime, the 0-0 transition is dipole forbidden, only allowed by thermal excitation or defects, and as a result, thin films have a 0-0/0-1 transition absorbance ratio of $\sim 0.5 - 0.8$. This aggregate type dominates due to amorphous chains reducing the polymer chain planarity and consequently, conjugation lengths. Electrospinning produces aggregates with greater J-type character, where the 0-0 transition is allowed, and in Fig. 5d, we observe a relative intensity of ~ 0.9 in absorbance between the two transitions. Here, the polymer chain backbones are more planarized with less perturbation from amorphous chains, leading to increased intrachain interactions.

Analysis of the spinning solution reveals that DMF addition, a non-solvent for P3HT, begins to induce the precipitation of aggregates, as the orange, translucent P3HT solution in chloroform, becomes an opaque, dark red/purple. In Fig. S15, vibronic peaks, associated with solid phase P3HT, appear alongside the π - π^* transition at 451 nm of the well-dissolved polymer. In fact, controlled use of an antisolvent is a known method for the production of self-assembled P3HT nanofibers [45]. Therefore, nanostructures have already begun to form even before electrospinning. Upon spin-coating these solutions, we notice the 0-0/0-1 peak ratio is similar for films cast with or without the non-solvent, retaining dominant H-aggregate behavior. This suggests the self-assembled nanostructures are either H-aggregates and electrospinning is required to introduce J-type features, or that the aggregate density is too high to detect them. Previous studies have shown J-aggregates to appear as H-type aggregates in concentrated solutions or dense films, as the sidechains can attenuate the intrachain order of surrounding aggregates [44].

Additionally, a red-shift was seen (0-0: 607 nm \rightarrow 613 nm, and 0-1: 556 nm \rightarrow 563 nm) in the absorbance traces in Fig. 5d upon electrospinning compared to thin-films cast by spin-coating. This shift arises as the spinning process elongates and planarizes the polymer backbone, increasing the conjugation length. With films, this is only achieved by energy-intensive thermal annealing processes. Due to the differences between the absorbance trace shapes, light harvesting was determined by integration of the absorbance area between 350 and 800 nm. This red-shift and enhanced 0-0 transition results in a lower energy absorption onset and thus greater harvesting by nanofibers between 550 and 650 nm, in comparison to the equivalent film, shown in Fig. 5g. This, and a higher absorption ‘tail’ below 450 nm, led to a 1.14x improvement in light harvesting of the P3HT fibers over the thin-film, rising from 31.2% to 36.6% (details in Fig. S16 and Table S4).

More significant enhancements were observed from the introduction of nanoparticles in Fig. 5e and h. Incorporated into electrospun P3HT fibers, the addition of PEO-reduced AgNPs and OA-capped AuNPs delivered a strong broadband enhancement across the entire visible light region versus pristine nanofibers, of 1.30x and 1.38x, respectively, however no evident enhancement was observed from OA-capped AgNPs (1.04x). Compared to the pristine P3HT films, the PEO-reduced AgNP and OA-capped AuNP-containing P3HT nanofibers provide an enhancement of 1.48x and 1.58x, respectively.

Diffuse reflectance spectroscopy of nanoparticle-containing PEO nanofibers revealed that the plasmonic absorbance for each nanoparticle type was retained upon electrospinning, indicating the potential to harness the LSPR effect. However, OA-capped NPs are more intensely plasmonic than PEO-reduced AgNPs (see Fig. S17c). It was therefore initially surprising to see PEO-reduced AgNPs deliver strong enhancement, given that we see no influence with OA-capped AgNPs. Due to their size, the nanoparticles do not scatter efficiently, [49] whilst, as the smallest, PEO-reduced AgNPs scatter the least. Therefore, we attempt to explain these observations with the longer wavelength, broad plasmon resonances of PEO-reduced AgNPs and OA-capped AuNPs, in comparison to OA-capped AgNPs. This provides a greater spectral overlap with the donor polymer, resulting in a stronger LSPR effect and superior absorption enhancement [50].

The peak position of plasmonic absorption is strongly dependent upon the refractive environment as shown by Finite-Difference Time-Domain (FDTD) simulations, used to solve the absorption and scattering spectra of the nanoparticles within the P3HT matrix (refractive index approximated to 1.95 [51, 52]). In Fig. S18, the plasmonic absorption of OA-capped AgNPs is expected at 480 nm, presenting a modest spectral overlap with the semiconductor. Meanwhile, the OA-capped AuNPs plasmon resonance is centered at 580 nm, overlapping well with the maximum absorption of the semiconductor. We also estimate that PEO-reduced AgNPs possess a greater spectral overlap with the surface plasmon resonance found at 520 nm within this refractive environment, calculated by blue shifting the OA-capped AgNP simulated spectra by 40 nm as observed when dispersed in chloroform.

Figure 5f and i shows that OA-capped AuNP infusion produced similar but lesser broadband enhancements within thin-films, whilst OA-AgNPs again had no influence. This disparity between the enhancement observed in fibers (1.38x) and in films (1.17x) (Fig. S16b-c) allows us to deconvolute the contributions of LSPR and electrospinning. The enhancement seen in thin films is assumed to originate only from plasmonic effects, meaning the

difference between the enhancement in fibers and films can be ascribed to the additional electrospinning-induced polymer alignment from the nanoparticle-driven diameter reductions. Therefore, we find that the photon absorption enhancement from the combination of these two approaches – electrospinning photoactive nanofibers and noble metal nanoparticle introduction, is synergistic, providing a greater joint enhancement than the sum of their individual parts.

3 Conclusions

We present a reduction of electrospun P3HT fiber diameters through nanoparticle-driven modulation of the viscosity and conductivity of the spinning solution. As a time-dependent process, we can control the fiber diameter by the age of the spinning solution, making it possible to identify the optimal time to produce the thinnest possible nanofibers. After removal of the sacrificial polymer, we achieve nanofiber diameters of 55 nm - the thinnest reported in the literature by 30%. Our fibers therefore offer the shortest diffusion pathways of excitons to the fiber surface, or heterojunction upon acceptor infiltration, and offer a crucial advancement towards achieving the ideal P3HT nanofiber for photovoltaic applications.

A dual-mode enhancement in light harvesting is identified from electrospinning-induced polymer chain alignment, and plasmonic effects from the nanoparticles, combining to provide a 1.58x integrated absorbance enhancement over the equivalent-volume pristine P3HT thin-films produced by spin-coating. We also reveal that the extent of polymer alignment is inversely proportional to the fiber diameter, which in turn increases photon absorption. The absorbance maximum increases by up to 1.84x from 45% to 83% upon nanoparticle-induced diameter reductions.

Whilst this work focuses on the well-studied polymer, P3HT, our system may be adapted to many donor-acceptor systems. The interplay between PEO and the nanoparticles dominates the electrospinning behavior, dictating the fiber diameter reductions and the resultant absorption enhancements. When using separately synthesized OA-capped NPs, the orthogonal solvent, DMF, can be omitted entirely with equal success. Therefore, the photoactive polymer may be switched out with other donor materials with the expectation of analogous results. The practical application of this strategy with these alternate systems should be the focus of future work to demonstrate this universality.

Additionally, the fibers shall be incorporated within active layers in order to translate the enhancement in absorption reported here into device efficiency improvements.

4 Experimental section/methods

This section describes the necessary materials and protocol to synthesize the lowest reported dimension of P3HT nanofibers to date. It covers the preparation of suitable nanoparticles for incorporation into ultra-thin nanofibers, the preparation of the spinning solution, the electrospinning process, and the post-processing PEO removal step. Details of how these nanofibers were characterized follows this protocol.

4.1 Chemicals and materials

Poly(3-hexylthiophene-2,5-diyl) (P3HT, M_w 50,000) was obtained from Rieke Metals. Poly(ethylene oxide) (PEO, M_w 900,000), chloroform, N-N'-dimethylformamide (DMF), isopropanol (IPA), silver nitrate (AgNO_3), tetrachloroauric(III) acid trihydrate ($\text{HAuCl}_4 \cdot 3\text{H}_2\text{O}$), oleylamine (OA, technical grade 70%), and methanol, were all obtained from Sigma Aldrich. Solvents were dried using molecular sieves and dissolved oxygen was removed by the freeze-pump-thaw method using a Schlenk line. Materials and samples were stored within a nitrogen-filled glovebox and protected from exposure to light where necessary.

4.2 Nanoparticle synthesis

OA-capped silver nanoparticles were produced by a modified 'solvent free' approach to the protocol outlined by *Hiramatsu and Osterloh* [53]. A solution of AgNO_3 (100 mg, 0.6 mmol) in oleylamine (2 mL, 4.2 mmol) was rapidly injected into additional oleylamine (15 mL, 32 mmol) heated to 175 °C in a round bottom flask. The color of the solution quickly turned yellow, and eventually to black. The solution was vigorously stirred for 10 minutes, and then allowed to cool to room temperature. Methanol (50 mL) was then added to precipitate the product. The particles were isolated by centrifugation and washed with methanol three times, before redispersion in chloroform. The synthesis was conducted under a nitrogen environment using a Schlenk line. Analogously, OA-capped gold nanoparticles could be obtained by using tetrachloroauric acid (100 mg, 0.3 mmol). TEM revealed that the OA-capped AgNP cores were 9.1 ± 2.7 nm, and OA-capped AuNPs were 10.4 ± 2.5 in diameter (see Fig. S19).

PEO-reduced AgNPs were prepared in-situ by direct addition of the silver salt dissolved in DMF to the spinning solution, following by heating at 40 °C for up to 96 h.

4.3 Electrospinning

In a typical experiment, the spinning solution was prepared by dissolving the photoactive polymer, P3HT (0.15 - 0.25 wt%), and auxiliary polymer, PEO (0.35 wt%), in

chloroform at 40 °C for 1 h. Following complete dissolution, AgNO_3 dissolved in DMF, or DMF and OA-capped NPs, were added dropwise to the polymer solution under vigorous stirring to prevent precipitation. The resultant chloroform:DMF solvent mixture contained 95:5 w/w. The spinning solution was then stirred for up to 96 h at 40 °C. AgNO_3 or OA-capped NP concentrations are typically given in weight percent with respect to the PEO concentration. The solution was drawn into a syringe and fed through a flat tip needle at 1 mL h⁻¹ (27-gauge) at 20 - 22 °C. A bias voltage of 23 kV was then applied between the stainless steel needle and a grounded plate collector at a separation of 20 cm. The as-spun nanofibers were then washed in IPA at 70 °C for 1 h to remove PEO, yielding dark-purple nanoparticle-containing P3HT nanofibers. All work was carried out within a nitrogen environment in a glovebox, however the nanofibers could also be prepared in air given a relative humidity of <20%.

Unless specified otherwise, nanoparticle additions of 5 wt% wrt PEO (of either AgNO_3 or OA-capped NPs) were made to 0.35 wt% PEO spinning solutions, 2 wt% wrt PEO additions to 1.5 wt% PEO solutions, and 10 wt% wrt PEO for P3HT/PEO solutions.

4.4 Characterization of nanofibers

Nanofiber morphology was analyzed using a Zeiss Merlin and JEOL JSM-840F SEM under an operating voltage of 4 kV. Specimens were sputter coated in 6 nm Pt prior to imaging. The nanofiber width, (fiber diameter parallel with the substrate) including coating, was determined from at least 100 unbiased counts from SEM micrographs using ImageJ software. Nanofiber height (fiber diameter normal to the substrate) was determined from vertical displacement profiles extracted from AFM images collected with an Agilent 5400 AFM. Nanoparticles, and the dispersion of nanoparticles within nanofibers, were examined on JEOL 3000F TEM at an accelerating voltage of 200 kV, fitted with a STEM unit ADF detector and Oxford Instruments EDX. BET analysis was carried out using a Micromeritics Gemini VII BET surface area analyzer using a N₂ absorptive. Samples were degassed under vacuum for 10 h before analysis.

The viscosity of spinning solutions was investigated using a Brookfield DV2T viscometer with a HA torque spring and CP4-41Z cone spindle, rotated at 30 rpm or 60 s⁻¹ shear rate. Electrical conductivity of solutions was found using an Oakton CON 550 Benchtop Conductivity Meter fitted with a K=0.1 cell at ambient conditions (20 ± 0.5 °C). Surface tension measurements were obtained using the pendant drop technique with an Ossila Contact Angle Goniometer under ambient conditions.

TGA was employed using a Perkin Elmer TGA 8000. Nanofiber samples were heated in air to 900 °C at 10 °C min⁻¹ to quantify nanoparticle retention upon

washing, or held at a 370 °C isotherm for 1 h under nitrogen to investigate PEO removal. FTIR attenuated total reflection (ATR) spectroscopy was recorded on a Varian Excalibur FTS 3500 FT-IR spectrometer. Due to strong light scattering of the nanomaterials, absorbance was determined by recording combined total transmittance and reflectance spectra using an Ocean Optics Flame Miniature Spectrometer equipped with DH-2000-BAL UV-VIS-NIR light source and ISP-50-8-R-GT Integrating Sphere. Thick P3HT films were spin-coated onto indium tin oxide (ITO) coated glass substrates, and nanofibers were prepared to the equivalent mass. The processed absorbance spectra were then smoothed using a Savitzky Golay Filter. Polarized absorption spectroscopy was employed by placing a Thorlabs film polarizer between the incumbent light and the fibers which were aligned using a rotating drum collector. The film was orientated so that the impinging light was polarized parallel and perpendicular to the fiber axes. The expected absorption and scattering spectra of nanoparticles dispersed within a P3HT medium were solved using Lumerical FDTD simulation software. XRD diffractograms were carried out using a Bruker D8 ADVANCE Eco diffractometer in reflection mode using a Ni-filtered Cu K α radiation. Again, films and fibers were prepared to the equivalent mass (~2 mg) by spin-coating or electrospinning directly onto a zero-background Si substrate. The background was removed, and peaks fitted using a Pearson VII function.

Supplementary Information The online version contains supplementary material available at <https://doi.org/10.1007/s42114-023-00788-0>.

Acknowledgements We thank Greg Cook and Richard Turner for their support in building the electrospinning apparatus. Special thanks to Professor Patrick Grant for providing access to the viscometer.

Authors' contributions RMS, BMM, HEA, NG designed the project, RMS conducted nanoparticle and fibre experiments and was supported by SD (fibers) and DMG (nanoparticles). Characterisation, data analysis and curation was done by RMS, and GTT (TEM). The first draft of the manuscript was prepared by RMS and all authors contributed to the review and editing. NG secured funding, provided infrastructure/resources, and HEA, RSB provided access to infrastructure/resources; Supervision by BMM, HEA, NG.

Funding The authors acknowledge use of characterization facilities with the Oxford Materials Characterization Service, and David Cockayne Centre for Electron Microscopy, Department of Materials, University of Oxford, alongside financial support provided by the Henry Royce Institute (EP/R010145/1). This work (RMS., GTT, DMG) was financially supported by the Engineering and Physical Sciences Research Council (EP/T517181/1) and by the Faraday Institution (NG, BMM and SD). NG thanks The Royal Society for the Royal Society Industry Fellowship. RSB was supported by the Royal Academy of Engineering under the Research Fellowship scheme (RF\201819\18\38).

Data availability The data that support the findings of this study are available from the corresponding authors upon reasonable request.

Declarations

Conflict of interest The authors declare that they have no conflict of interest.

Open Access This article is licensed under a Creative Commons Attribution 4.0 International License, which permits use, sharing, adaptation, distribution and reproduction in any medium or format, as long as you give appropriate credit to the original author(s) and the source, provide a link to the Creative Commons licence, and indicate if changes were made. The images or other third party material in this article are included in the article's Creative Commons licence, unless indicated otherwise in a credit line to the material. If material is not included in the article's Creative Commons licence and your intended use is not permitted by statutory regulation or exceeds the permitted use, you will need to obtain permission directly from the copyright holder. To view a copy of this licence, visit <http://creativecommons.org/licenses/by/4.0/>.

References

- van Bavel S, Sourty E, de With G, Frolic K, Loos J (2009) Relation between photoactive layer thickness, 3D morphology, and device performance in P3HT/PCBM bulk-heterojunction solar cells. *Macromolecules* 42:7396–7403. <https://doi.org/10.1021/ma900817t>
- Mihaiilechi VD, Xie HX, de Boer B, Koster LJA, Blom PWM (2006) Charge Transport and Photocurrent Generation in Poly(3-hexylthiophene): Methanofullerene Bulk-Heterojunction Solar Cells. *Adv Funct Mater* 16:699–708. <https://doi.org/10.1002/adfm.200500420>
- Ma W, Yang C, Gong X, Lee K, Heeger AJ (2005) Thermally stable, efficient polymer solar cells with nanoscale control of the interpenetrating network morphology. *Adv Funct Mater* 15:1617–1622. <https://doi.org/10.1002/adfm.200500211>
- Kim Y, Choulis SA, Nelson J, Bradley DDC, Cook S, Durrant JR (2005) Device annealing effect in organic solar cells with blends of regioregular poly(3-hexylthiophene) and soluble fullerene. *Appl Phys Lett* 86:063502. <https://doi.org/10.1063/1.1861123>
- Li G, Yao Y, Yang H, Shrotriya V, Yang G, Yang Y (2007) “Solvent annealing” effect in polar solar cells based on poly(3-hexylthiophene) and Methanofullerenes. *Adv Funct Mater* 17:1636–1644. <https://doi.org/10.1002/adfm.200600624>
- Park JH, Kim JS, Lee JH, Lee WH, Cho K (2009) Effect of annealing solvent solubility on the performance of poly(3-hexylthiophene)/Methanofullerene solar cells. *J Phys Chem* 113:17579–17584. <https://doi.org/10.1021/jp9029562>
- Jo J, Na S-I, Kim S-S, Lee T-W, Chung Y, Kang S-J, Vak D, Kim D-Y (2009) Three-dimensional bulk heterojunction morphology for achieving high internal quantum efficiency in polymer solar cells. *Adv Funct Mater* 19:2398–2406. <https://doi.org/10.1002/adfm.200900183>
- Park SY, Labanti C, Luke J, Chin Y-C, Kim J-S (2022) Organic bilayer photovoltaics for efficient indoor light harvesting. *Adv Energy Mater* 12:2103237. <https://doi.org/10.1002/aenm.202103237>
- Lenes M, Koster LJA, Mihaiilechi VD, Blom PWM (2006) Thickness dependence of the efficiency of polymer:fullerene bulk heterojunction solar cells. *Appl Phys Lett* 88:243502. <https://doi.org/10.1063/1.2211189>
- Shaheen SE, Brabec CJ, Sariciftci NS, Padinger F, Fromherz T, Hummelen JC (2001) 2.5% efficient organic plastic solar cells. *Appl Phys Lett* 78:841–843. <https://doi.org/10.1063/1.1345934>

11. Dong S, Maciejewska B, Millar R, Grobert N (2023) 3D electrospinning of Al₂O₃/ZrO₂ fibrous aerogels for multipurpose thermal insulation. *Adv Compos Hybrid Mater*. <https://doi.org/10.21203/rs.3.rs-3164092/v1>
12. Yarin AL, Zussman E (2004) Upward needleless electrospinning of multiple nanofibers. *Polymer* 45:2977–2980. <https://doi.org/10.1016/j.polymer.2004.02.066>
13. Lukas D, Sakar A, Pokorny P (2008) Self-organization of jets in electrospinning from free liquid surface: a generalized approach. *J Appl Phys* 103:084309. <https://doi.org/10.1063/1.2907967>
14. Bedford NM, Dickerson MB, Drummy LF, Koerner H, Singh KM, Vasudev MC, Durstock MF, Naik RR, Steckl AJ (2012) Nanofiber-based bulk-heterojunction organic solar cells using coaxial electrospinning. *Adv Energy Mater* 2:1136. <https://doi.org/10.1002/aenm.201100674>
15. Huang HJ-N, Nan HR, Yang YG, Gao XY, Chen F, Chen Z-K (2018) Improved performance of thick films based binary and ternary bulk heterojunction organics photovoltaic devices incorporated with electrospinning processed nanofibers. *Adv Mater Interfaces* 5:1800914. <https://doi.org/10.1002/admi.201800914>
16. Kim T, Yang SJ, Kim SK, Choi HS, Park CR (2014) Preparation of PCDTBT nanofibers with a diameter of 20 nm and their application to air-processed organic solar cells. *Nanoscale* 6:2847–2854. <https://doi.org/10.1039/c3nr05539h>
17. Kim T, Yang SJ, Sung SJ, Kim YS, Chang MS, Jung H, Park CR (2015) Highly reproducible Thermocontrolled electrospun Fiber based organic photovoltaic devices. *ACS Appl Mater Interfaces* 7:4481–4487. <https://doi.org/10.1021/am508250q>
18. Yoon S, Han Y, Hwang I (2018) Probing molecular orientation of P3HT nanofibers in Fiber-based organic solar cells. *Electron Mater Lett* 14:46–51. <https://doi.org/10.1007/s13391-017-7155-9>
19. Kim T, Im JH, Choi HS, Yang SJ, Kim SW, Park CR (2011) Preparation and photoluminescence (PL) performance of a nanoweb of P3HT nanofibers with diameters below 100 nm. *J Mater Chem* 21:14231–14239. <https://doi.org/10.1039/c1jm10396b>
20. Erb T, Raleva S, Zhokhavets U, Gobsch G, Stühn B, Spode M, Ambacher O (2004) Structural and optical properties of both pure poly(3-octylthiophene) and P3OT/fullerene films. *Thin Film Solids* 450:97–100. <https://doi.org/10.1016/j.tsf.2003.10.045>
21. Pierini F, Lanzi M, Nakielski P, Pawlowska S, Urbanek O, Zembrzycki K, Kowalewski TA (2017) Single-material organic solar cells based on electrospun fullerene-grafted Polythiophene nanofibers. *Macromolecules* 50:4972–4981. <https://doi.org/10.1021/acs.macromol.7b00857>
22. Lee S, Moon GD, Jeong U (2009) Continuous production of uniform poly(3-hexylthiophene) (P3HT) nanofibers by electrospinning and their electrical properties. *J Mater Chem* 19:743–748. <https://doi.org/10.1039/b814833c>
23. Dillard C, Singhal R, Kalra V (2015) Hierarchical self-assembly in Monoaxially electrospun P3HT/PCBM nanofibers. *Macromol Mater Eng* 300:320–327. <https://doi.org/10.1002/mame.201400214>
24. Sundarajan S, Murugan R, Nair AS, Ramakrishna S (2010) Fabrication of P3HT/PCBM solar cloth by electrospinning technique. *Mater Lett* 64:2369–2372. <https://doi.org/10.1016/j.matlet.2010.07.054>
25. Yoon R, Ji S, Yoo Y, Jeong J-E, Kim J, Woo HY, Park B, Hwang I (2016) Enhanced polarization ratio of electrospun nanofibers with increased Intrachain order by Postsolvent treatments. *J Phys Chem B* 120:12981–12987. <https://doi.org/10.1021/acs.jpcc.6b08277>
26. Ahmad H, Zhang S, Liu C-T, Ma G, Azoulay JD, Gu X, Hangishetty MK, Kundu S (2022) Effect of poly(3-hexylthiophene) molecular weight and the aging of spinning solution on the Electrospun Fiber properties. *ACS Appl Polym Mater* 4:8812–8824. <https://doi.org/10.1021/acsapm.2c01229>
27. Arrigoni A, Brambilla L, Castiglioni C, Bertarelli C (2022) Conducting electrospun nanofibers: monitoring of iodine doping of P3HT through infrared (IRAV) and Raman (RaAM) Polaron spectroscopic features. *Nanomaterials* 12:4308. <https://doi.org/10.3390/nano12234308>
28. Papaparaska G, Papagiorgis P, Itskos G, Krasia-Christoforou T (2022) Highly aligned electrospun polymer fibers produced using a corrugated static collector. *ACS Appl Polym Mater* 4:586–597. <https://doi.org/10.1021/acsapm.1c01435>
29. Reneker DH, Yarin AL (2008) Electrospinning jets and polymer nanofibers. *Polymer* 49:2387–2425. <https://doi.org/10.1016/j.polymer.2008.02.002>
30. Dong S, Maciejewska BM, Lißner M, Thomson D, Townsend D, Millar R, Petrinic N, Grobert N (2023) Unveiling the mechanism of the *in situ* formation of 3D Fiber macroassemblies with controlled properties. *ACS Nano* 17:6800–6810. <https://doi.org/10.1021/acsnano.3c00289>
31. Kim C-H, Cha S-H, Kim SC, Song M, Lee J, Shin WS, Moon S-J, Bahng JH, Kotov NA, Jin S-H (2011) Silver nanowire embedded in P3HT:PCBM for high-efficiency hybrid photovoltaic device applications. *ACS Nano* 5:3319–3325. <https://doi.org/10.1021/nn200469d>
32. Wang DH, Kim JK, Lim G-H, Park KH, Park OO, Lim B, Park JH (2012) Enhanced light harvesting in bulk heterojunction photovoltaic devices with shape-controlled ag nanomaterials: ag nanoparticles *versus* ag nanoplates. *RSC Adv* 2:7268–7272. <https://doi.org/10.1039/c2ra20815f>
33. Wu J-L, Chen F-C, Hsiao Y-S, Chien F-C, Chen P, Kuo C-H, Huang MH, Hsu C-S (2011) Surface Plasmonic effects of metallic nanoparticles on the performance of polymer bulk heterojunction solar cells. *ACS Nano* 5:959–967. <https://doi.org/10.1021/nn102295p>
34. Xue M, Li L, Tremolet de Villers BJ, Shen H, Zhu J, Yu Z, Stieg AZ, Pei Q, Schwartz BJ, Wang KL (2011) Charge-carrier dynamics in hybrid plasmonic organic solar cells with ag nanoparticles. *Appl Phys Lett* 98:253302. <https://doi.org/10.1063/1.3601742>
35. Kim K, Carroll DL (2005) Roles of au and ag nanoparticles in efficiency enhancement of poly(3-octylthiophene)/C₆₀ bulk heterojunction photovoltaic devices. *Appl Phys Lett* 87:203113. <https://doi.org/10.1063/1.2128062>
36. Saquing CD, Manasco JL, Khan SA (2009) Electrospun nanoparticle-nanofiber composites via a one-step synthesis. *Small* 5:944–951. <https://doi.org/10.1002/smll.200801273>
37. Tijng LD, Ruelo MTG, Amarjargal A, Pant HR, Park C-H, Kim CS (2012) One-step fabrication of antibacterials (silver nanoparticles/poly(ethylene oxide)) – polyurethane bicomponent hybrid nanofibrous mat by dual-spinneret electrospinning. *Mater Chem Phys* 134:557–561. <https://doi.org/10.1016/j.matchemphys.2012.03.037>
38. Chang H-C, Liu C-L, Chen W-C (2013) Flexible Nonvolatile Transistor Memory Devices Based on One-Dimensional Electrospun P3HT: Au Hybrid Nanofibers. *Adv Funct Mater* 23:4960–4968. <https://doi.org/10.1002/adfm.201300283>
39. Senses E, Ansar SM, Kitchens CL, Mao Y, Narayanan S, Natarajan B, Faraone A (2017) Small particle driven chain disentanglements in polymer nanocomposites. *Phys Rev Lett* 118:147801. <https://doi.org/10.1103/PhysRevLett.118.147801>
40. Senses E, Kitchens CL, Faraone A (2022) Viscosity reduction in polymer nanocomposites: insights from dynamic neutron and X-ray scattering. *J Polym Sci* 60:1130–1150. <https://doi.org/10.1002/pol.20210320>
41. Wu B, Wu X, Guan C, Tai KF, Yeow EKL, Fan HJ, Matthews N, Sum TC (2012) Uncovering loss mechanisms in silver nanoparticle-blended plasmonic organic solar cells. *Nat Commun* 4:02004. <https://doi.org/10.1038/ncomms3004>
42. Xu X, Jiang L, Zhou Z, Wu X, Wang Y (2012) Preparation and properties of electrospun soy protein isolate/polyethylene oxide

- nanofiber membranes. *Appl Mater Interfaces* 4:4331–4337. <https://doi.org/10.1021/am300991e>
43. Johnston DE, Yager KG, Hlaing H, Lu X, Ocko BM, Black CT (2014) Nanostructures surfaces frustrate polymer semiconductor molecular orientation. *ACS Nano* 8:243–249. <https://doi.org/10.1021/nn4060539>
 44. Niles ET, Roehling JD, Yamagata H, Wise AJ, Spano FC, Moulé AJ, Grey JK (2012) J-aggregate behavior in Poly-3-hexylthiophene nanofibers. *J Phys Chem Lett* 3:259–263. <https://doi.org/10.1021/jz201509h>
 45. Roehling JR, Arslan I, Moulé AJ (2012) Controlling microstructure in poly(3-hexylthiophene) nanofibers. *J Mater Chem* 22:2498–2506. <https://doi.org/10.1039/c2jm13633c>
 46. Jo G, Jung J, Chang M (2019) Controlled self-assembly of conjugated polymers via a solvent vapor pre-treatment for use in organic field-effect transistors. *Polymers* 11:332. <https://doi.org/10.3390/polym11020332>
 47. Spano FC, Silva C (2014) H- and J-aggregate behavior in polymeric semiconductors. *Annu Rev Phys Chem* 65:477–500. <https://doi.org/10.1146/annurev-physchem-040513-103639>
 48. Spano FC (2010) The spectral signatures of Frenkel Polarons in H- and J-aggregates. *Acc Chem Res* 43:429–439. <https://doi.org/10.1021/ar900233v>
 49. Dong S, Tebbutt TT, Millar R, Grobert G, Maciejewska BM (2023) Hierarchical porosity design enables highly recyclable and efficient au/TiO₂ composite fibers for photodegradation of organic pollutants. *Mater Des* 234:112318. <https://doi.org/10.1016/j.matdes.2023.112318>
 50. Liu S-Y, Huang L, Li J-F, Wang C, Li Q, Xu H-X, Guo H-L, Meng Z-M, Shi Z, Li Z-Y (2013) Simultaneous excitation and emission enhancement of Fluorescence assisted by double Plasmon modes of gold Nanorods. *J Phys Chem C* 117:10636–10642. <https://doi.org/10.1021/jp4001626>
 51. Petoukhoff CE, O'Carroll DM (2015) Absorption-induced scattering and surface plasmon out-coupling from absorber-coated plasmonic metasurfaces. *Nat Commun* 6:7899. <https://doi.org/10.1038/ncomms8899>
 52. Morfa AJ, Barnes TM, Ferguson AJ, Levi DH, Rumbles G, Rowlen KL, van de Lagemaat J (2011) Optical characterization of pristine poly(3-hexyl thiophene) films. *J Polym Sci B Polym Phys* 49:186–194. <https://doi.org/10.1002/polb.22183>
 53. Hiramatsu H, Osterloh FE (2004) A simple large-scale synthesis of nearly monodisperse gold and silver nanoparticles with adjustable sizes and with exchangeable surfactants. *Chem Mater* 16:2509–2511. <https://doi.org/10.1021/cm049532v>
- Publisher's Note** Springer Nature remains neutral with regard to jurisdictional claims in published maps and institutional affiliations.